# X-Raying the hot gas in the outskirts of galaxy clusters

Zhu, Z.

# 1 Introduction

## 1.1 Galaxy clusters and the intracluster medium

The first written reference to a cluster of galaxies can be traced back to the French astronomer Charles Messier in 1780s (Messier 1781). The study of galaxy clusters, particularly prominent nebulae clusters, underwent a transformation in the 1920s with Edwin Hubble's demonstration that spiral and elliptical nebulae are actual galaxies, similar to the Milky Way but situated at large distances from us. His work in 1926 suggested that galaxy clusters are systems of enormous size (Hubble 1926). Shortly after Zwicky's discovery of dark matter in the Coma Cluster (Zwicky 1933, further elaborated in Zwicky 1937), clusters have become fundamental elements for cosmological studies. The original catalog of 2712 nearby rich clusters of galaxies was published in 1958 by George O. Abell (Abell 1958), which laid a solid foundation for the development of research on clusters. A review by Biviano (2000) covers more details of early stage astrophysics research on galaxy clusters from 1784 to 1983.

Modern observational studies have revolutionized our understanding of galaxy clusters. Galaxy clusters are unique laboratories for studying plasma physics. Approximately 80-90% of the baryonic mass in massive galaxy clusters resides in the intracluster medium (ICM) (Gonzalez et al. 2007, 2013; Chiu et al. 2016), which is generally well described as a hot ($10^7$–$10^8$ K), optically-thin, collisionally ionized, low-density ($10^{-5}$–$10^{-3}$ cm$^{-3}$) plasma. The thermal plasma emission in galaxy clusters can be observed in X-rays, for instance, the central gaseous emission in Abell 2744 taken with the *Chandra* telescope (see Figure 1.1). With the on-duty X-ray telescopes *Chandra* and *XMM-Newton*, the gas temperature and density

profiles can be well measured via imaging and spectral analysis from the core regions out to intermediate radii. At larger radii, however, such measurements become challenging as the X-ray emission gets much fainter (See Section 1.2).

### 1.1.1 X-ray emission from hot gas

The main radiative processes for the X-ray bright ICM are thermal bremsstrahlung for the continuum and excitation processes from various chemical elements for the line emission. In relatively low-temperature environments, two photon emission and radiative recombination also become important for the continuum emission (See Kaastra et al. 2008, for a review). In the presence of strong shocks, non-thermal bremsstrahlung further contributes to the continuum. Acceleration models predict that the electrons have a power-law distribution in energy, resulting in power-law shape spectra, which can be seen as a hard X-ray tail superimposed on the curved bremsstrahlung spectrum of the bulk of the hot electrons (Kaastra et al. 1999). Not accounting for such components may lead to an overestimation of the plasma temperature.

The hot ICM permeating galaxy clusters has been continuously enriched by metals synthesized in Type Ia and core-collapse supernovae. The presence and intensity of Fe-K lines (6.4–7.0 keV) are used to diagnose high-temperature plasma, widely detected in the spectra of objects such as active galactic nuclei (AGN), supernova remnants (SNR), and hot galaxy clusters, while Fe-L lines (0.7–1.5 keV) are effective in diagnosing lower-temperature plasma. With the high energy resolution brought by the recently launched X-Ray Imaging and Spectroscopy Mission (XRISM), the Fe-K line complex can be well resolved into individual lines, and the kinematics of different gas components can be measured.

### 1.1.2 ICM thermodynamic and chemical properties

In preparation for exploring the ICM properties, it is crucial to obtain an accurate measurement of the cluster mass. Assuming the gas is in hydrostatic equilibrium with the gravitational potential, we can derive the mass profile of a galaxy cluster based on the observed temperature and density profiles of the ICM. The total mass enclosed within radius r in a cluster can

be estimated via:

$$M_{tot}(< r) = -\frac{r^2 k_B T_{gas}(r)}{G\mu m_p}\left(\frac{d\ln n_{gas}(r)}{dr} + \frac{d\ln T_{gas}(r)}{dr}\right), \tag{1.1}$$

where $m_p$ is the proton mass and $\mu$ is the mean molecular weight of the gas, $T_{gas}(r)$ and $n_{gas}(r)$ represent the gas temperature and density at radius $r$ (Ettori et al. 2013). However, this method may lead to biased mass estimation due to hydrostatic non-equilibrium, non-thermal pressure, projection effects, and observational uncertainties in the temperature and density profiles. The weak gravitational lensing (WL) analysis serves as a more robust tool to map the mass distribution, since it has no assumption for the dynamical state (See Bartelmann & Schneider 2001, for a review). This technique works by statistically measuring subtle distortions in the shapes of distant galaxies caused by the gravitational field of massive objects. The precise WL mass measurements for cluster catalogues (e.g. Mandelbaum et al. 2018; McClintock et al. 2019; Murray et al. 2022) laid a solid foundation for the studies of the ICM properties.

In cases where no WL measurement is available and X-ray data is insufficient to obtain the mass profile, scaling relations between observable quantities and cluster mass are widely used to derive the cluster mass. In early studies of galaxy clusters, the X-ray temperature was considered as a reliable mass proxy (Smith et al. 1979; Ikebe et al. 2002). More recently in Arnaud et al. (2010), ten nearby relaxed clusters have been used to derive the $M_{500}$–$T_x$ scaling relation with *XMM-Newton* data. Later on, with deeper *XMM-Newton* observations and the recent all-sky survey by extended ROentgen Survey with an Imaging Telescope Array (eROSITA; launched in 2019), much larger samples of clusters have been analyzed to constrain this scaling relation. Figure 1.2 shows the measurements from the eROSITA Final Equatorial-Depth Survey (eFEDS) and the comparison between various $M_{500}$–$T_x$ relations derived from different samples of clusters (Chiu et al. 2022). Other scaling relations of cluster X-ray luminosity, gas mass, and derived quantities with cluster mass have also been thoroughly studied (Mantz et al. 2016; Bulbul et al. 2019; Chiu et al. 2022).

It is interesting to study the thermodynamic properties (e.g. temperature, density, pressure and entropy) of the ICM, which reveal crucial insights into the formation, evolution, and physical conditions of galaxy clusters. Assuming hydrostatic equilibrium for the cluster gas, the thermodynamic properties are expected to be uniform across different azimuthal directions within a narrow radial shell. However, both simulations and X-ray

observations show that the ICM is continuously perturbed by large-scale accretion, mergers and other turbulent motions such as sloshing, AGN feedback and thermal instabilities (see Walker et al. 2019b; Simionescu et al. 2019, for a review). The thermodynamical profiles measured in clusters are expected to be close to self-similar once scaled by the cluster mass, therefore the self-similar model of clusters introduced by Kaiser (1986) has been widely used as a baseline model. Comparing the observed thermodynamic profiles to predictions of baseline models can help to isolate the impact of more complex physical processes in cluster formation.

Precise abundance measurements of all the metals from O to Fe, Ni enable us to understand the chemical evolution history of the clusters. Previous studies on metallicity spatial distribution has shown that metals are not distributed uniformly near the cluster cores (e.g. Simionescu et al. 2009; Lovisari et al. 2009). However, at large radii (i.e. beyond 0.4 $R_{500}$), the metallicity profiles of both relaxed and disturbed systems show a flat distribution: a constant value of $0.3 \pm 0.1$ $Z_{\odot}$ (Lovisari & Reiprich 2019). For the analysis in all chapters of this thesis, we adopted the abundance table from Lodders et al. (2009) unless otherwise stated.

### 1.1.3 Dynamical features in the ICM

Relying on imaging and spectroscopic analyses (e.g. investigating the surface brightness perturbations and properties of the emission lines), we are able to probe the ICM gas motions. With *Chandra* and *XMM-Newton* mapping, dynamic features in the ICM such as shocks and cold fronts have been identified and thoroughly studied in a large amount of galaxy clusters. Across the shock fronts, both temperature and density of the gas will decrease from the downstream to the upstream region (See Markevitch & Vikhlinin 2007, for a review). Using *XMM-Newton* observations on the nearby merging cluster Abell 3667, Finoguenov et al. (2010) discovered the first shock in the merging clusters co-located with cluster radio shocks (relics). This result has later been confirmed by Akamatsu et al. (2012) using *Suzaku* data. Subsequent studies have constently detected such shocks in various merging clusters (Akamatsu et al. 2013; Ogrean et al. 2013; Botteon et al. 2016; Hoang et al. 2018; Urdampilleta et al. 2018).

It is noteworthy that the observed prominent sharp X-ray brightness edges are not only associated with shock waves but can also be related to cold fronts. *Chandra* observations unveiled the cold fronts for the first time in the merging cluster Abell 2142 (Markevitch et al. 2000). As opposed to

shocks, the gas on the denser side of cold fronts would show a lower temperature compared to that on the upstream side, while maintaining continuous pressure across both sides. Both shocks and cold fronts are good indicators of past dynamic events in the clusters.

The Mach number of a shock, a dimensionless quantity defined as the ratio of the speed of the shock wave to the sound speed, is widely used to describe the strength of a shock. Based on the X-ray measured temperature and density breaks, we can estimate the Mach number of the shock assuming the Rankine-Hugoniot conditions. The Rankine-Hugoniot relations (Macquorn Rankine 1870) describe the conservation of mass, momentum, and energy across a shock front, predicting and relating the discontinuity of density and temperature when the shock wave passes through an ideal gas and compresses it.

## 1.2 The outskirts of galaxy clusters

### 1.2.1 Physically important scales and radii in the outskirts

The mass of the cluster is usually quoted within an overdensity radius $r_N$ as $M_N = (4\pi/3)N\rho_{crit}(z)r_N^3$, where $\rho_{crit}$ is the critical density of the universe at the redshift z of the cluster. The critical density is the mean density of matter required for gravity to halt the expansion of the universe. The defined $r_N$ is the radius within which the mean density is $N \times \rho_{crit}$. $r_{500}$ and $r_{200}$ are two most frequently used radii in the studies of the clusters. $r_{500}$ roughly marks the radius out to which the cluster temperature and gas density could be measured with on-duty *Chandra* and *XMM-Newton* telescopes. $M_{500}$ is defined accordingly as the cluster mass within $r_{500}$. $r_{200}$, commonly referred to as virial radius $R_{vir}$, has historically been used as an approximation of the virial radius ($r_{18\pi^2} \approx r_{178}$) assuming an Einstein-de Sitter Universe ($\Omega_m = 1$). In the Lambda Cold Dark Matter ($\lambda$CDM) model, however, the virial radius is closer to $r_{110}$. As predicted by simulation results (Molnar et al. 2009), the positions of the virial shocks in clusters usually fall between 1-1.5 $R_{vir}$ with a Mach number of 2.5–4. The virial shocks, with an aspherical curved feature as marked in Figure 1.3, heat the hot baryons as they fall into the gravitational potential. The external accretion shock (Ryu et al. 2003; Molnar et al. 2009), which is located farther out at $\sim 3R_{vir}$ and characterized by a very large Mach number ($\approx$100), plays an important role to heat the infalling low density gas into a hot and dif-

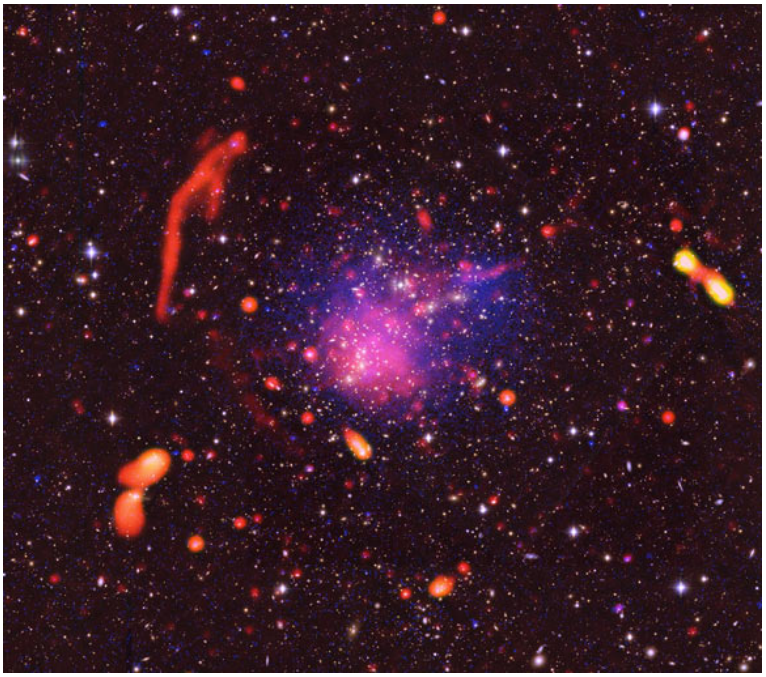

**Figure 1.1:** Optical, radio and X-ray composite images of the galaxy cluster Abell 2744. The central X-ray emission (shown in blue) from the thermal ICM is observed by *Chandra* in the 0.5–2.0 keV band. The shock waves in the cluster have set off a celestial fireworks display of bright radio emission (shown in red; measured by 1–4 GHz Very Large Array (VLA)), tracing cosmic rays and magnetic fields. Credit: Pearce et al. (2017) / NRAO / AUI / NSF / *Chandra* / Subaru / ESO.

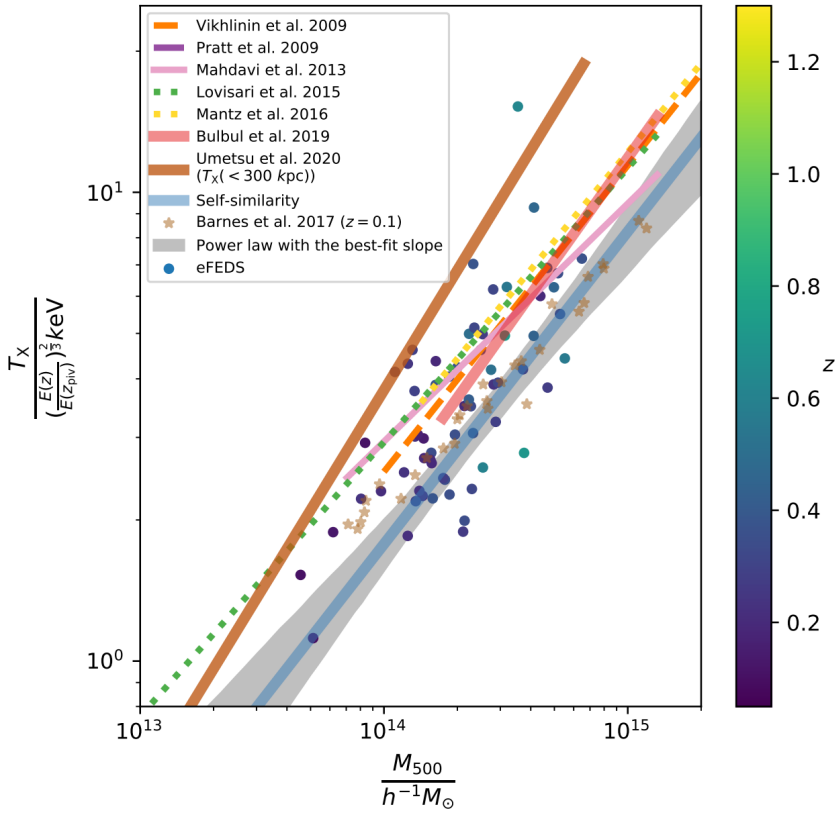


**Figure 1.2:** Comparison between the eFEDS sample and the $M_{500}$–$T_X$ scaling relations from the literature. The eFEDS clusters are shown by the circles color coded by the redshift. The Hubble parameter is $H_0 = h \times 100$ km s$^{-1}$ Mpc$^{-1}$ with $h = 0.7$. $E(z) = \sqrt{\Omega_m(1+z)^3 + \Omega_\Lambda}$ is the ratio of the Hubble constant at redshift z with its present value. Credit: Chiu et al. (2022).

fuse state. By definition, the region between $r_{500}$ and the external accretion shock is called the outskirts.

### 1.2.2 Methods for exploring the cluster outskirts

X-ray observations serve as an efficient tool to study the cluster outskirts, allowing us to analyze the temperature, density and chemical composition of the ICM. The Suzaku telescope (2005-2015), benefiting from its relative low and stable particle background and high effective area, enabled studies of a long list of clusters out to their virial radii including Abell 2204 (Reiprich et al. 2009), Abell 1795 (Bautz et al. 2009), Abell 1413 (Hoshino et al. 2010), Abell 1689 (Kawaharada et al. 2010), Abell 2142 (Akamatsu et al. 2011), Hydra A (Sato et al. 2012), Abell 2029 (Walker et al. 2012b), the Coma Cluster (Simionescu et al. 2013), the Centaurus Cluster (Walker et al. 2013) and the Perseus Cluster (Simionescu et al. 2011; Urban et al. 2014). A more complete list can be found in Table 1 of Walker et al. (2019b). However, its large point spread function (PSF$\sim$2′) largely precludes us from probing surface brightness breaks which indicate shocks or cold fronts.

Benefiting from the high spatial resolution, *Chandra* and *XMM-Newton*, both launched in 1999, have also significantly contributed to our understanding of galaxy cluster outskirts by providing detailed views of the ICM, revealing fine dynamical structures in the outskirts such as shock waves and cold fronts. More recently, with the new availability of the eROSITA All-Sky Survey (eRASS, Predehl et al. 2021) in the 0.2–10 keV X-ray band, sensitive studies of the diffuse emission in the cluster outskirts (out to $\sim 1.5R_{200}$) have been carried out in nearby bright clusters such as Coma and Virgo (Churazov et al. 2021; McCall et al. 2024).

However, sometimes it can be very challenging to study the cluster outskirts with X-ray observations. X-ray emissivity is always proportional to the square of the plasma density, therefore the X-ray signal decreases rapidly as the density drops from $\sim 10^{-1}$ cm$^{-3}$ in the cluster cores to $\sim 10^{-5}$ cm$^{-3}$ near the virial radius. A proper handling of the instrumental and sky background as well as the associated systematic uncertainties becomes extremely important for the X-ray studies in the outskirts (see Section 1.2.3 for more detailed discussion). As a powerful complementary tool to the X-ray observations, the thermal Sunyaev-Zeldovich effect (SZ effect; Sunyaev & Zeldovich 1972) has played a crucial role for probing the cluster outskirts. The cosmic microwave background (CMB) radiation interacts with hot electrons in galaxy clusters, resulting in a characteristic shift in the

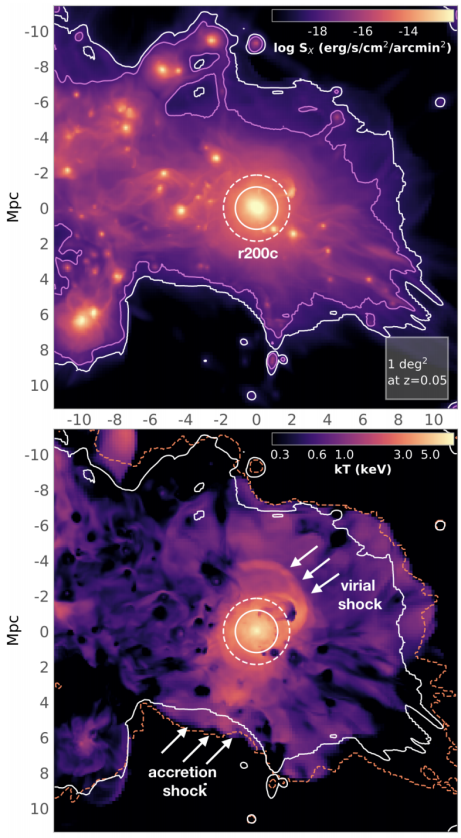


**Figure 1.3:** Example of a massive, relatively relaxed cluster from the *Omega500* adiabatic cosmological simulation (Nelson et al. 2014). *Top:* predicted X-ray emissivity in the 0.5–2 keV band. Purple contours show $S_X \geqslant 2 \times 10^{-19}$ erg s$^{-1}$ cm$^{-2}$ arcmin$^{-2}$. Solid and dashed circles show $r_{500c}$ and $r_{200c}$, respectively. *Bottom:* projected temperature map. Credit: Simionescu et al. (2019).

CMB spectrum through inverse Compton scattering. The surface brightness of the thermal SZ effect has a linear dependence on thermal electron pressure, which diminishes slower compared to X-ray signal towards the outskirts. The Planck satellite, the South Pole Telescope (SPT) and the Atacama Cosmology Telescope (ACT) have accurately measured cluster pressure profiles. The XMM-Newton Cluster Outskirts Project (X-COP; Eckert et al. 2017), taking advantage of high spatial resolution X-ray observations in combination with the SZ imaging technique, offered a complementary view of the physical conditions in the cluster outskirts (Ghirardini et al. 2018).

### 1.2.3 Background handling for X-ray spectral analysis

Due to the weak X-ray signal in the cluster outskirts, we should more carefully deal with the instrumental/particle backgrounds and sky backgrounds. The X-ray foreground and background spectral model consists of four components: a power-law for the cosmic X-ray background (CXB) from unresolved point sources, and three thermal components representing the Galactic halo (GH, Kuntz & Snowden 2000), a patchy $\sim$0.6 keV hot foreground (HF, Yoshino et al. 2009) from the Milky Way, and the local hot bubble (LHB, Sidher et al. 1996). The contribution of GH and LHB has been frequently constrained by ROSAT All Sky Survey (RASS) these days, however in the future, better estimation can be provided by eRASS. We can estimate the unresolved CXB flux with *cxbtool* (Mernier et al. 2015; de Plaa 2017), by integrating the best-fit derivative source luminosity function (dN/dS) of *Chandra* Deep Field South (CDFS; Lehmer et al. 2012) data. However, if the spectral extraction region is too small, the cosmic variance will become very high, leading to large systematic uncertainties in the measured thermodynamic profiles. The particle background, also called as instrumental background or non X-ray background (NXB) is produced by high-energy charged particles hitting the detector from random angles. Therefore, the spectral shape and flux of the particle background varies depending on the design of the satellite and its radiation environment. In some cases, the observations after light curve screening still suffer from residual soft proton flare (SPF) contamination, the soft and highly temporally variable component of the particle background (Kuntz & Snowden 2008). To eliminate the contamination of SPF, we can model this component with a power-law (or broken power-law) model not folded through the instrumental effective areas and fit simultaneously with the source spectra.

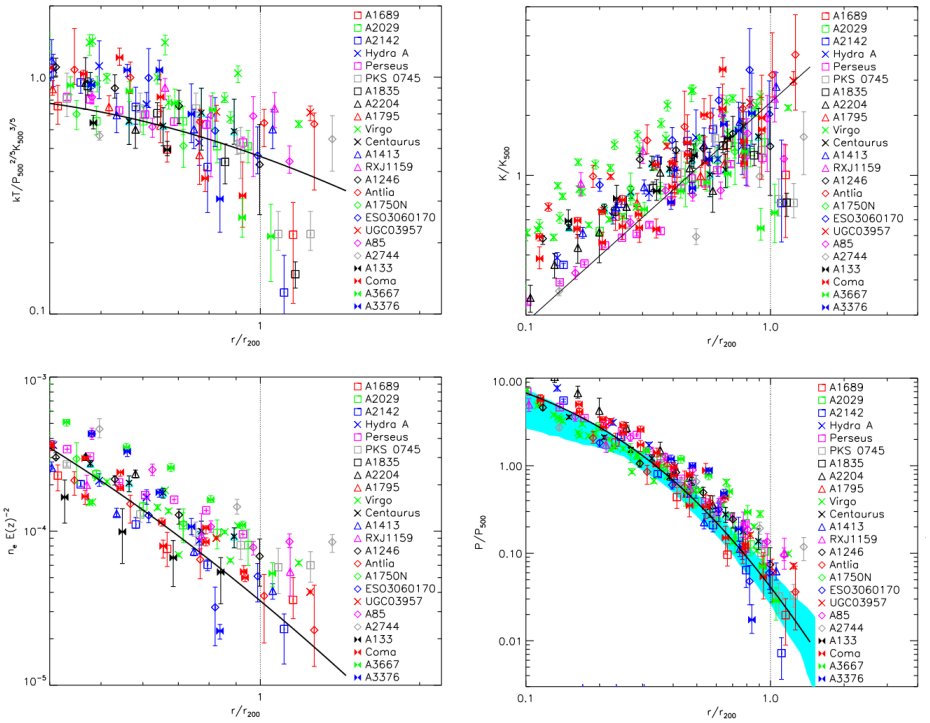


**Figure 1.4:** *Top Left:* The self-similarly scaled Suzaku temperature profiles in the outskirts. *Top Right:* Entropy profiles scaled by self-similar entropy at $R_{500}$ with comparison to the baseline entropy profile (black line). The characteristic entropy $K_{500}$ scales with the cluster mass: $K_{500} = 106\,\mathrm{keV\,cm^2}\left(\frac{M_{500}}{10^{14}\mathrm{M}_\odot}\right)^{\frac{2}{3}}\left(\frac{1}{f_\mathrm{b}}\right)^{\frac{2}{3}}E(z)^{-\frac{2}{3}}$ (Voit et al. 2005; Pratt et al. 2010). *Bottom Left:* Self-similarly scaled Suzaku density profiles in the outskirts. *Bottom Right:* The self-similarly scaled Suzaku pressure profiles are compared to the universal pressure profile (black line) and the range of the Planck cluster pressures profiles (cyan region). The characteristic pressure is defined as $P_{500} = 1.65\times10^{-3}\,E(z)^{\frac{8}{3}}\left[\frac{M_{500}}{3\times10^{14}h_{70}^{-1}\mathrm{M}_\odot}\right]^{\frac{2}{3}}h_{70}^2\,\mathrm{keV\,cm^{-3}}$ (Nagai et al. 2007). Credit: Walker et al. (2019b).

### 1.2.4 Gas clumping

While the ICM has been commonly assumed to be a single temperature medium with uniform density in X-ray analysis, it can be very inhomogenous (i.e., 'clumpy') which leads to an overestimation of the gas density by $\sqrt{C(r)}$, where C $\equiv \langle\rho^2_{gas}\rangle/\langle\rho_{gas}\rangle^2$. Numerical simulations predict that the gas density distribution becomes increasingly clumpy towards the outskirts of the cluster (Nagai & Lau 2011).

This prediction has been supported by the thermodynamic profiles of the ICM measured from X-ray observations. Figure 1.4 shows the analysis of a sample of 24 clusters studied by *Suzaku* in the outskirts (Walker et al. 2013, 2019b). As mentioned in Section 1.1.2, the thermodynamic profiles are expected to be self-similar and exhibit little cluster-to-cluster variation, making them well-suited to be described with baseline profiles. The baseline entropy profile, following a power-law distribution, is predicted from simulations assuming purely gravitational collapse (Voit et al. 2005; Pratt et al. 2010). The generalized NFW pressure profile proposed by Nagai et al. (2007) is utilized as the baseline pressure model, with parameters derived from fitting observations of 33 nearby clusters using *XMM-Newton* data (Arnaud et al. 2010). The observed entropy profiles rise from the cluster core, get flat outside $r_{500}$ and lie below the baseline model in the outskirts. The tendency for the gas density to become higher than the baseline model aligns well with the increasingly clumpy nature of the cluster outskirts predicted by simulation results.

In Zhuravleva et al. (2013), an innovative method has been raised to identify and characterize the structure of ICM in simulated galaxy clusters. Simulation results show that the distribution of gas properties in a given radial shell can be well described by a log-normal probability density function and a tail. The clumps can thus be easily selected corresponding to the tail of this distribution (see Figure 1.5). This method has been applied to study the gas clumping in the Virgo cluster(Mirakhor & Walker 2021), where a relatively mild level of gas clumping ($\sqrt{C} < 1.1$) has been reported in the outskirts towards the north.

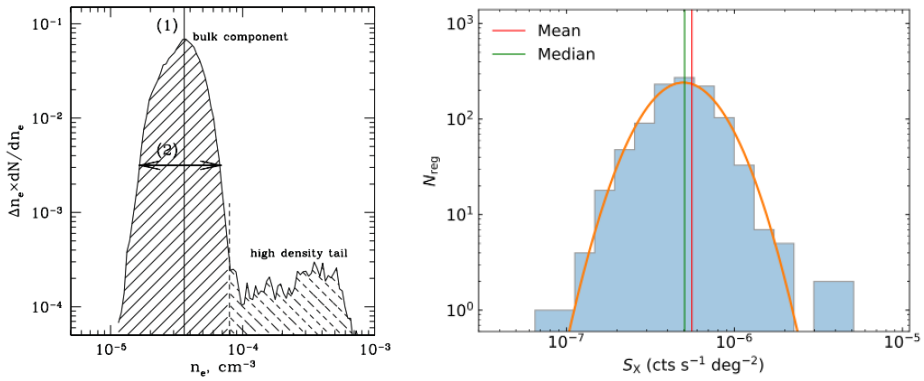


**Figure 1.5:** *Left:* The probability density function (PDF) of the ICM density in a radial shell at 1.1–1.2 $r_{500}$ in a simulated relaxed cluster. The distribution is composed of two components: bulk, volume-filling component and high-density inhomogeneities, occupying small fraction of the shell volume (Zhuravleva et al. 2013). *Right:* Distribution of the X-ray surface brightness for the region along the northern strip of the Virgo cluster, showing that the observed surface brightness distribution of the ICM can be divided into a bulk component and a high-density tail resulting from gas clumping.The median surface brightness (green line) coincides better with the peak of the best-fit log-normal model compared to the mean (red line) (Mirakhor & Walker 2021).

## 1.3 Non-thermal view of galaxy clusters

### 1.3.1 Diffuse radio emission

A large variety of diffuse synchrotron sources populate galaxy clusters, uncovering the non-thermal content of the ICM: cosmic rays (CRs) electrons and weak magnetic fields ($\sim 0.1 - 10\mu$Gauss) (Brüggen et al. 2012). Overviews of the theoretical frameworks (Brunetti & Jones 2014) and observational reviews (van Weeren et al. 2019a; Paul et al. 2023) describe in detail the formation mechanisms for the diffuse radio emission in galaxy clusters. While different generation mechanisms have been proposed, the observed spectra are mostly quite steep, with spectral indices $\alpha \leqslant -1$ (e.g., see the compilation by Duchesne et al. 2021). Due to their steep radio spectra, diffuse cluster sources are best detected at low frequencies. Recent upgrades to facilities such as the Karl G. Jansky Very Large Array (Perley et al. 2011) and the Giant Metrewave Radio Telescope (uGMRT; Gupta et al. 2017), along with the emergence of new-generation interferometers such as the LOw Frequency ARray (LOFAR; van Haarlem et al. 2013), MeerKAT (Jonas 2009), the Murchison Widefield Array (MWA; Tingay et al. 2013) and the Australian Square Kilometre Array Pathfinder (ASKAP; Hotan et al. 2021), have greatly improved the sensitivity to probe diffuse radio sources.

Diffuse radio emission can be classified into three broad classes (van Weeren et al. 2019a):

- **Radio halos** are extended sources centrally located in merging clusters, following the ICM baryonic mass distribution. These objects can be further classified as giant radio haloes and mini-halos depending on their sizes.

- **Radio relics** have been defined as megaparsec-sized diffuse sources tracing (re-)accelerated particles by shock waves. Cluster radio relics are mostly located on the periphery of the cluster, which typically have a convex morphology with respect to the cluster centre and exhibit a radio spectral steepening towards the cluster centre. Most of them are observed to be highly polarised (20–30% at 1.4 GHz; Kierdorf et al. 2017; Stuardi et al. 2019). As shown in Figure 1.6, the "toothbrush" cluster (RX J0603.3+4214) and the "sausage" cluster

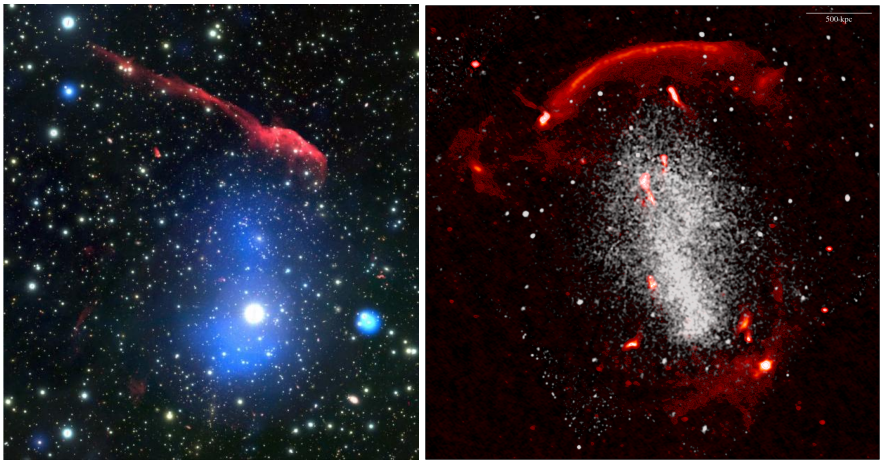


**Figure 1.6:** *Left:* A multiwavelength false-color image of the "Toothbrush" cluster, 1RXS J0603.3+4214 (van Weeren et al. 2016). The stem of the brush is from radio emission (red) while the toothpaste is produced by X-rays observed by *Chandra* (blue). *Right:* The merging galaxy cluster CIZA J2242.8+5301, nicknamed as the "Sausage", is well-known for its giant radio relic in the north. The cluster also hosts extremely hot gas in the cluster centre, observed with *Chandra* X-ray observations (in white; Ogrean et al. 2013). Image credits: Duy Hoang/LOFAR Surveys Team.

(CIZA J2242.8+5301) are the templates of clusters hosting prominent radio relics.

- **Revived AGN fossil plasma / phoenices** refer to AGN radio plasma that has been re-energized in the ICM. Although these sources exhibit irregular filamentary morphologies, they are characterized by the ultra-steep radio spectra ($\alpha < -1.5$) and their AGN origins. Phoenices (Kempner & David 2004) usually locate closer to the cluster core and have smaller sizes ($\leqslant$ 300-400 kpc) compared to radio relics.

### 1.3.2 Merger shocks and radio relics

Cluster mergers are the most energetic events since the Big Bang, releasing a large amount of energy ($\sim 10^{64}$ ergs) into the cluster environment and playing a key role in the evolution of galaxy clusters (Sarazin 2002; Hoeft et al. 2008). The shocks, cold fronts and turbulence generated by the mergers will propagate through the hot, diffuse ICM.

As illustrated in Figure 1.7, different stages of merger evolution exhibit shocks at various locations. In the early stages of a merger, simulations predict a pair of shocks propagating outward along the equatorial plane of the merger (Ha et al. 2018). Using *Chandra*/*XMM-Newton*/*Suzaku* X-ray observations, Gu et al. (2019) identified the first rare equatorial shock in the pre-merger cluster pair 1E 2216 and 1E 2215, confirming this important merging epoch just before core collision. In the late phase of the merger, after the two dark matter cores have passed each other and the gas clumps have merged, the launched axial shocks move in opposite directions along the merger axis.

A portion of the energy dissipated by merger shocks accelerates cosmic ray electrons through the diffusive shock acceleration (DSA) (Bell 1978; Drury 1983; Blandford & Eichler 1987). In $\sim \mu$Gauss intracluster magnetic fields, the relativistic electrons radiate via synchrotron emission and create elongated diffuse radio features called radio relics. The relation between radio relics and shocks has been well established through multiple shocks observed in X-rays, identified as discontinuities in the density and temperature profiles of the ICM at the positions of relics (e.g. Markevitch & Vikhlinin 2007; Akamatsu et al. 2017; Zhang et al. 2021).

Key open questions regarding radio relics include: (1) why there is a discrepancy between the Mach numbers of shock waves derived from X-ray and radio observations in many cases (e.g. van Weeren et al. 2016; Hoang et al. 2018; Stuardi et al. 2019), and (2) how weak shocks with low Mach numbers could accelerate particles from thermal pools to relativistic energies and later create radio relics. While DSA is a powerful mechanism for particle acceleration, its application to weak shocks (with Mach number $\mathcal{M} < 2.25$; Ryu et al. 2019) faces challenges in terms of acceleration efficiency. The most viable solution is the re-acceleration mechanism, which has been proposed for multiple systems such as A3411-3412 (van Weeren et al. 2017), PLCK G287.0+32.9 (Bonafede et al. 2014), RXC J1314.4-2515 (Stuardi et al. 2019) and CIZA J2242.8+5301 (Di Gennaro et al. 2018). In this scenario, the aged fossil plasma gets re-accelerated by the shock waves and therefore form a radio relic with a morphology following the distribution of the seed population.

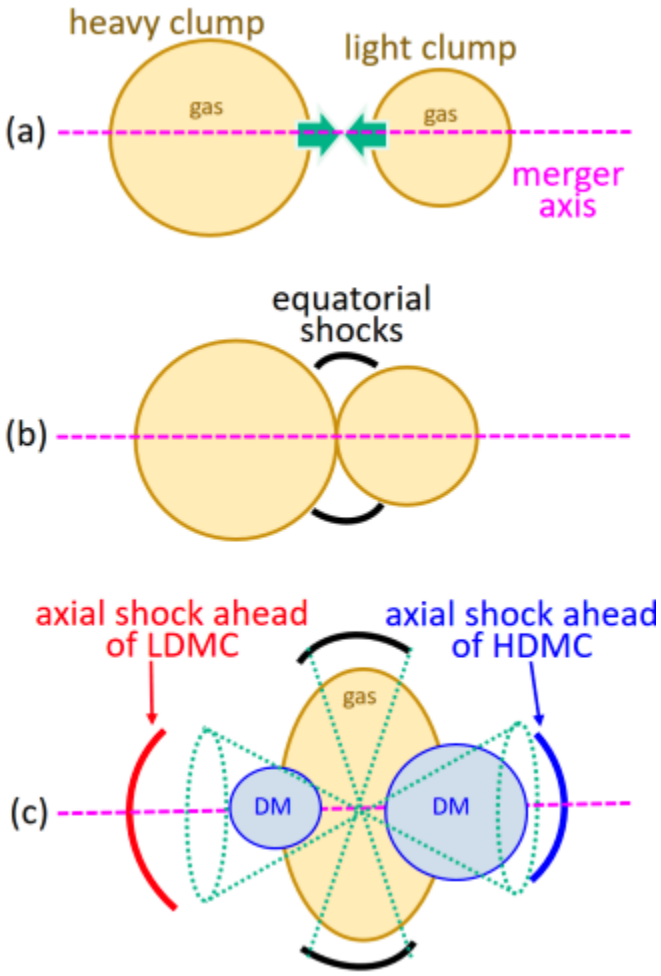


**Figure 1.7:** Schematic illustration of merger evolution for an idealized binary merger. (a) Heavy and light gas clumps undergo a head-on collision. (b) The equatorial shocks expand outwards along the direction perpendicular to the merger axis. (c) The axial shocks launch in the opposite direction along the merger axis and the two gas clumps merge into a single core. Credit: Ha et al. (2018).

## 1.4 Thesis outline

This thesis focuses on the X-ray analysis of hot intra-cluster medium in galaxy clusters, particularly in the outskirts. This work deepens the understanding of the ICM thermodynamic properties in the outskirts of clusters, and further explores the thermal and non-thermal features in merging clusters.

Chapter 2 reports an unprecedented virial shock candidate in the Perseus Cluster with *Suzaku* observations. The location of this shock near the virial radius ($\sim r_{200}$) towards the northwest, coincides well with the break in the projected temperature profile and the discontinuity of the density profiles. The Mach number derived from the X-ray temperature break and the scaled radius of this shock reported here indeed lie within the range for "virial shocks" as predicted in Molnar et al. (2009). Although virial shocks are not typically expected to be found in the inner $r_{200}$ region, the shock shape can be significantly aspherical, especially in a cluster like Perseus where signs of asymmetry on large scales are present out to very large radii. Regardless of its exact nature, the detection of this shock paves the way for understanding the heating processes that are at play in the outer parts of galaxy clusters, where the ICM meets the surrounding large-scale structure.

Chapter 3 presents the gas clumping study in the outskirts of Abell 133 with unique mapping from *Suzaku* and *Chandra*. An increase of the gas clumping at larger radii can lead to significant systematic biases in the X-ray measurements of various ICM properties, for instance, leading to overestimations of the density and, consequently, underestimation of the gas entropy. To precisely correct the thermodynamic profiles for this gas clumping effect, we attempted to identify significant clumps based on *Chandra* images and mask them in the *Suzaku* spectral analysis. Counterintuitively, the 16 *Chandra* selected clump candidates are mainly projected background objects instead of genuine inhomogeneity. For the case of Abell 133, even after the correction for the clumping resolved by ultra-deep *Chandra* data, we still see an entropy deficit and a density excess compared to the expectations. This suggests that the unresolved clumping and other physical mechanisms (e.g., non-thermal pressure or non-equilibrium electrons in the ICM) in the outskirts may play an additional role to bias the thermodynamic profiles.

In Chapter 4, we probed the gas clumping in the outskirts of another

bright nearby cluster, Abell 1795. With special coverage from *Chandra* and *Suzaku* out to very large radii even beyond the virial radius, Abell 1795 is the most ideal target apart from Abell 133 (see Chapter 3) to investigate the impact of gas clumps on the observed surface brightness and thermodynamic profiles. We identified 24 clump candidates in the Abell 1795 field, most of which are likely to be associated with background objects. Upon removal of clump candidates from the ICM, the emissivity bias profile flattens at $\sim$1, indicating no or only marginal unresolved clumping remained in Abell 1795. After removing all detected *Chandra* sources (including both point sources and clump candidates), the entropy profile of the ICM still departs from what is expected from a purely gravitational infall, indicating more complex physics at play in the outskirts. These findings shed new light on ICM clumping studies and provide a robust foundation for the development of next-generation cosmological simulations. **In this collaboration, I did all the data reduction, imaging and spectral analysis of the *Suzaku* observations on Abell 1795. I also contributed on the method of clump identification, analysis of surface brightness profile and thermodynamic profiles and relevant discussion.**

In Chapter 5, we investigated a unique merging cluster PSZ2G181.06+48.47, a low-mass cluster that hosts double radio relics located far from each other. Using newly obtained X-ray observations taken from *Chandra* and *XMM-Newton*, we identified two surface brightness breaks in the north-east (NE) and south-west (SW). The absence of an actual density jump gives an upper limit of $\mathcal{M}_X < 1.4$ for the SW shock and $\mathcal{M}_X < 1.8$ for the NE shock. Combining the radio observations of LOFAR, new VLA and uGMRT, we not only confirmed the double radio relics from the morphology but also obtained the spectral index map where clear steepening towards the cluster center has been observed for the SW relic. We proposed a late-stage merger scenario for this system, in which the shock front produced during the first encounter is propagating towards the outskirts, re-accelerating the local fossil plasma and creating the relics. PSZ2G181.06+48.47 is representative of more such low-mass systems to be discovered in the future, posing a firm challenge to our expectations that particle acceleration would be inefficient at low velocity shocks. **In this work, the radio data analysis was done by my collaborator Kamlesh Rajpurohit.**

## 1.5 Future prospects

**XRISM**
We are stepping into the era of XRISM, which has been successfully launched on September 7 in 2023. As the successor of ASTRO-H (*Hitomi* satellite), XRISM opens up a new world of high resolution X-ray spectroscopy. The onboard micro-calorimeter (*Resolve*) has achieved an amazing resolution of $< 5$ eV in the 0.3–12 keV energy range. Currently with the closed gate valve, however, photons at energies $\leqslant$2 keV are largely suppressed. The fresh exciting results from the high spectral resolution micro-calorimeter will come along in the following months. With the unprecedented resolving power, XRISM is able to precisely measure the gas motion and turbulence in merging clusters, placing better constraints on merger scenarios.

**NewAthena**
NewAthena will carry an X-ray micro calorimeter (X-IFU) and a wide field CCD imager (WFI) like XRISM, but is expected to achieve much higher sensitivity and spatial resolution. This mission, planned to launch by 2037, retains almost all of the Athena (Advanced Telescope for High ENergy Astrophysics; originally selected in 2014) science and aims to address new questions raised over the past decade. The key capabilities of the X-IFU lie in its unprecedented spectral resolution, better than 4 eV up to 7 keV, combined with a large effective area, in a $4'$ hexagonal field of view (the equivalent diameter) and a low instrumental background. With X-IFU, the gas kinematics will be spatially mapped with greater detail and coverage out to larger radii and higher redshifts compared to XRISM/*Resolve*, due to its higher sensitivity. Moreover, the thermodynamic and chemical properties of the ICM will also be precisely measured in the outskirts of clusters with NewAthena.

**HUBS**
The Hot Universe Baryon Surveyor (HUBS) mission is primarily designed to conduct a census of baryons in the warm-hot intergalactic media (WHIM). The results are expected to revolutionize our understanding of galaxy formation and directly address the issue of "missing baryons". With its unprecedented spatially-resolved high-resolution spectroscopy and large field of view, the HUBS mission will be uniquely qualified to measure the thermodynamical properties of the multi-phase gas from galactic to cosmolog-

ical scales. By measuring the metallicity and chemical composition of the ICM, HUBS will also provide insights into the enrichment history of galaxy clusters, including the role of supernovae and AGN feedback in distributing metals to the outskirts. To achieve the unprecedented energy resolution of 2eV in the 0.1–2 keV soft X-ray band, detectors needs to work in the extremely low temperature environment below 100mK, placing a high requirement for cryogenics.

**LEM**

The Line Emission Mapper (LEM) is an X-ray Probe proposed for the 2030s (not approved yet), which mainly aims to study the galaxy formation (Kraft et al. 2022). The ICM abundances and dynamical information out to $R_{200}$ are also major science drivers for LEM. The onboard microcalorimeter array/IFU will reach an unprecedented spectral resolution of 1.3 eV for the central 5′ and 2.5 eV for the rest of the field of view (FOV). Grasp is defined as the product of the effective area and the FOV, which is a sensitive indicator of the ability to probe the faint diffuse emission. LEM will have more than an order of magnitude larger grasp than Athena XIFU and more than three orders of magnitude larger grasp than XRISM Resolve.

**Table 1.1:** Parameters comparison between XRISM, NewAthena, HUBS and LEM

| Mission | Detector | Launch Date | Spectral Resolution | $A_{eff}$@0.5 keV | $\Omega_{FOV}(\mathrm{deg}^2)$ |
|---|---|---|---|---|---|
| XRISM | Resolve | 2023 | 100 | 50 | 0.0023 |
| NewAthena | X-IFU | ∼2037 | 240 | 6000 | 0.0069 |
| HUBS | XQSC | >2030 | 300 | 500 | 1 |
| LEM | IFU | 2032 | 300 | 1200 | 0.25 |

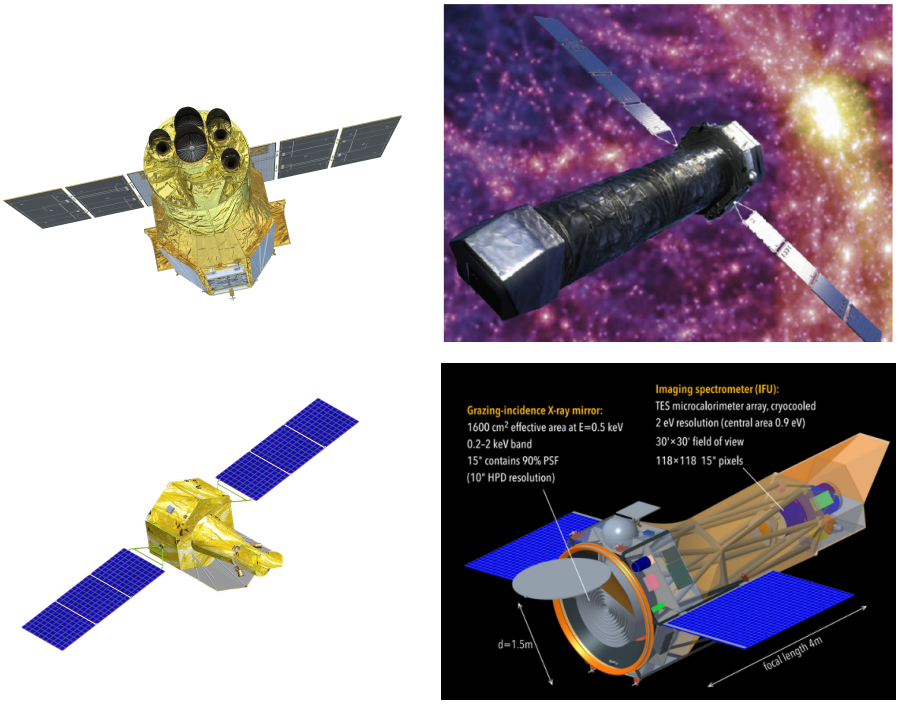


**Figure 1.8:** *Top Left:* Illustration of the *XRISM* satellite. Credit: JAXA/NASA *Top Right: NewAthena* telescope. Credit: ESA. *Bottom Left:* Hot Universe Baryon Surveyor (HUBS). Credit: Tsinghua University. *Bottom Right:* Line Emission Mapper(LEM). Credit: CfA/NASA.